Exploring the capabilities of scanning microwave microscopy to characterize semiconducting polymers

Olivier Douhéret, Didier Theron, David Moerman

applied sciences

MDPI

Article

Exploring the Capabilities of Scanning Microwave Microscopy to Characterize Semiconducting Polymers

Olivier Douhéret [1,*], Didier Théron [2] and David Moerman [1]

[1] Materia Nova R&D Center, Avenue Nicolas Copernic 3, B-7000 Mons, Belgium; david.moerman@materianova.be

[2] University Lille, CNRS, Centrale Lille, University Polytechnique Hauts-de-France, UMR 8520-IEMN, F-59000 Lille, France; didier.theron@univ-lille.fr

* Correspondence: olivier.douheret@materianova.be

Received: 27 October 2020; Accepted: 16 November 2020; Published: 20 November 2020

Featured Application: High resolution electrical characterization of organic semiconducting materials and structures—Microwave probing techniques for the description of mesoscopic mechanisms governing charge transport in organic semiconductors.

Abstract: Standing at the meeting between solid state physics and optical spectroscopy, microwave characterization methods are efficient methods to probe electronic mechanisms and mesoscopic transport in semiconducting polymers. Scanning microwave microscopy, augmented with a Mach-Zehnder interferometer detection unit to allow for the probing of high impedance structures was applied on poly(3-hexylthiophene-2,5-diy) and exhibited high sensitivity while operating at the nanoscale. Provided a well-defined experiment protocol, S_{11} phase and amplitude signals are shown to lead simultaneously yet independently to probing the variations of the dielectric properties in the materials, i.e., conductive and capacitive properties, respectively, upon applied DC gate bias. Adjusting the operating microwave frequency can also serve to probe carrier trapping mechanisms.

Keywords: scanning microwave microscopy; organic photovoltaics; charge transport; Mach-Zehnder interferometer detection unit

1. Introduction

The increasing demand for sustainable and renewable energy to cope with incoming crucial environmental challenges has been promoting alternative photovoltaic technologies since the turn of the century. Today, the most promising ones are standing on the brink of industrial development. Additionally, despite pending issues such as durability, photovoltaic technologies exhibiting specification such as low fabrication cost, lightweight, mechanical flexibility, low environmental impact and short energy payback time can now be foreseen in a near future with specific cases of use. These technologies are very diverse and based on many different types of materials and combinations with continuous development towards higher performing devices. Among them, hybrid perovskite and bulk heterojunction organic photovoltaic (OPV) technologies count among the most promising, considering the achieved performances and the huge scientific forces at work to conceive materials and unravel their complex properties [1–4]. This therefore requires high-resolution characterization techniques among which microwave-based methods were recently proven efficient for probing conductive properties of semiconducting materials [5–9] in addition the initial craze involving macroscale techniques since the beginning of the century [10–13]. As these techniques are sensitive to the loss of reflected transmitted microwaves in a (semi-)conducting medium and can be carried out without mechanical contacts, remote measurements can be considered on structures capped with encapsulating layers, as required in these devices to ensure sufficient stability.

This also makes them suitable techniques for future implementation in industrial environments as in-line feedback tools in process evaluation. Scanning microwave microscopy (SMM) consists of a microwave-based probing method integrated in a scanning probe microscope [14–20], thus allowing for two-dimensional mapping of electronic properties at the nanoscale. It can be used to investigate dielectric [21–23] and conductivity [24–26] properties. On organic-inorganic trihalides perovskites, Kelvin Force Microscopy (KFM) was also proposed to correlate the material's (photo)conductivity with its structural and morphological properties as they are well known to strongly affect the performances of the corresponding photovoltaic devices [27]. Meanwhile, the ability of dielectric resonators to electrically characterize organic conductors was demonstrated to operate at 9 GHz on a benzothiophene derivative [13]. Similar quantitative studies at the nanoscale are, however, lacking. In this work, SMM is applied on poly(3-hexylthiophene-2,5-diy) (P3HT) [1]. P3HT remains a reference hole transporting a semiconducting polymer in OPV, as the combination of the relative stability, the nanostructural tunability [28] and the decreasing production costs of the material with the sufficient photovoltaic performances of the devices, make it a pertinent case-study for material validations later to be extended to more specific structures as foreseen in different industrial applications. As the sensitivity of SMM to the variations of electrical properties in P3HT is observed, the choice of experimental parameters and the mechanisms ruling the different S_{11} signals recorded by the Keysight Power Network Analyzer (PNA) must be elucidated to reach meaningful properties of the materials under study. Different key parameters including the microwave frequency and the operating setpoint compared to the adjacent frequency are explored. SMM capability to probe simultaneously and independently GHz dielectric properties, i.e., microwave conductive and capacitive mechanisms is evidenced. These mechanisms include depth probing, mesoscopic transport and trapping mechanisms, thus demonstrating versatile capability for the study of OPV thin films both in scientific and industrial operating environment.

2. Experiment

Regioregular P3HT (average Mw 50,000–100,000) was purchased from Sigma-Aldrich/Merck and dissolved in anhydrous chlorobenzene, C_{P3HT}~20 mg mL^{-1}. The solution was stirred and heated at 70 °C overnight prior to spincoating at 700 rpm on a glass/ITO/MoO_3 substrates. 10 min annealing on a hot plate (Präzitherm) at 110 °C ensures complete evaporation of the solvent and crystallization of the film. The resulting film thickness is about 200 nm. The glass substrates with patterned Indium Tin Oxide (ITO) were purchased from Naranjo B.V. (ref. NS1463, t_{ITO} ~95 nm, ~20 Ω.□). A 10 nm MoO_3 layer was deposited by sublimation in a high vacuum evaporating chamber (Spectros, Kurt J. Lesker) at ~10^{-6} mBar, prior to spincoating the P3HT. A 10 nm thick and dense Al_2O_3 encapsulation grown at ~70 °C in primary vacuum (~1 mBar) by atomic layer deposition (Savannah 100, Cambridge Nanotech) completes the structure. Prior to SMM measurements the samples were pasted onto a conducting chuck to which the ITO layer was wired by means of Ag epoxy (RS). Apart from steps in vacuum, the preparation procedure was carried out in inert atmosphere (N_2) in a glovebox with less than 10 ppm of residual O_2 and H_2O, to prevent any exposure to air, and possibly alteration of the materials properties prior to measurements.

Microwave electrical characterization was carried out using a scanning microwave microscope from Keysight, equipped with a performance network analyzer (PNA). The detection unit was augmented with a home-made Mach-Zehnder interferometer to allow for 50 Ω free detection system [14], operating over a 2 to 18 GHz bandwidth and suitable for the study of such high impedance materials as P3HT. Full platinum-iridium tip probes (Ref. 12Pt400A) from Rocky Mountain Nanotechnology specifically designed for Keysight's SMM were used. A schematic of the SMM experimental set-up is presented in Figure 1a. Prior to any adjustment of the interferometer, the tip is put in contact with the sample. The deflection setpoint is adjusted to keep contact in the nN range and prevent any damage of the sample and deformation of the tip apex. The Atomic Force Microscope (AFM) is used in spectroscopy mode with no scanning to keep the probe still to perform the measurements. The impinging microwave (Power: 0 dBm) is first split in two waves and coupled back after reflection

of one of them at the tip sample contact as shown in Figure 1a and leading to the typical interferometric PNA amplitude and phase profile displayed in Figure 1b. A variable attenuator set in the pathway of the other wave serves to adjust the interferometric profile to lower the S_{11} parameter (down to −70 dB typically) as much as possible at the interferometric frequencies. This is required to achieve significant sensitivity. Because of the very low signal coming out of the interferometer, a 2–18 GHz band amplifier (Microsemi AML218L2502, 30 dB gain, 3 dB noise figure and 14 dBm output power at 1 dB gain compression) is added. The interferometric frequencies are detected at minimum PNA amplitude where a 180° phase shift is observed as explained below. The one at 10.46925 GHz is further highlighted in Figure 1c in semilog scale, and in linear scale in the inset. Practically, near an interference frequency f_0, the S_{11} parameter measured by the VNA can be approximately modeled by $S_{11} \cong A\Gamma_0 i \sin[\pi(f - f_0)(t_2 - t_1)]e^{-i\pi(f-f_0)(t_1+t_2)}$, where A contains average gain and phase shift throughout the circuit, t_1 and t_2 are the times needed for the microwave signal to travel the two branches of the interferometer and Γ_0 is the reflection coefficient of the device that allows the interferometer signal to be cancelled (see S6 on interferometer modeling). Curve fitting allows estimating $t_1 - t_2 \cong 10.9$ ns and $t_1 + t_2 \cong 28.4$ ns indicating a periodicity for the amplitude of about 100 MHz and for the phase of about 35 MHz. Therefore, for a few tens of kHz around f_0, the linear variations of the PNA amplitude validates the approximation $\sin x \cong x$ in the above equation in this narrow spectral range, confirming f_0 and the minimum amplitude. Additionally, when the frequency is swept around f_0, S_{11} vanishes at $f = f_0$ and changes of sign, which translates into a 180° phase shift. The logarithmic and linear displays of the PNA amplitude are correlated by the relation: PNA amp linear = 10^(PNA amp in dB/20). For the sake of simplicity, all PNA amplitude interferometric and time profiles will be displayed in logarithmic scale, with units in dB. The operating frequency f_{OP} is chosen in the vicinity (max ±10 kHz) of f_0, close enough to ensure maximum sensitivity variations of both phase and amplitude with material perturbations and far enough to prevent contrast reversal during measurements as f_0 slightly drifts and takes over f_{OP} in the measurement set (i.e., the frequency of operation is chosen to ensure that the measurement remains on one side of the interferometric frequency). This small drift yet detrimental artifact, typically between 1 to 100 Hz s^{-1}, is minimized by mounting the probes at least the day before the measurements. The drift is also evaluated prior to and/or during the measurements, to be removed upon the compilation of the results. The perturbation is a negative DC bias applied to the probe keeping the chuck and connected ITO electrode grounded. As P3HT is a p-type organic semiconductor, holes are the majority carriers and can be injected upon a negative DC tip bias (i.e., the gate bias). Hence, locally, the AFM tip/Al_2O_3/P3HT configuration forms a local Metal/Insulator/Semiconductor (MIS) junction. A periodic step variation of this DC gate bias between 0 V and the setting value is applied with a frequency of 100 mHz to ensure that space charge equilibrium is reached in the material between carrier injection and extraction.

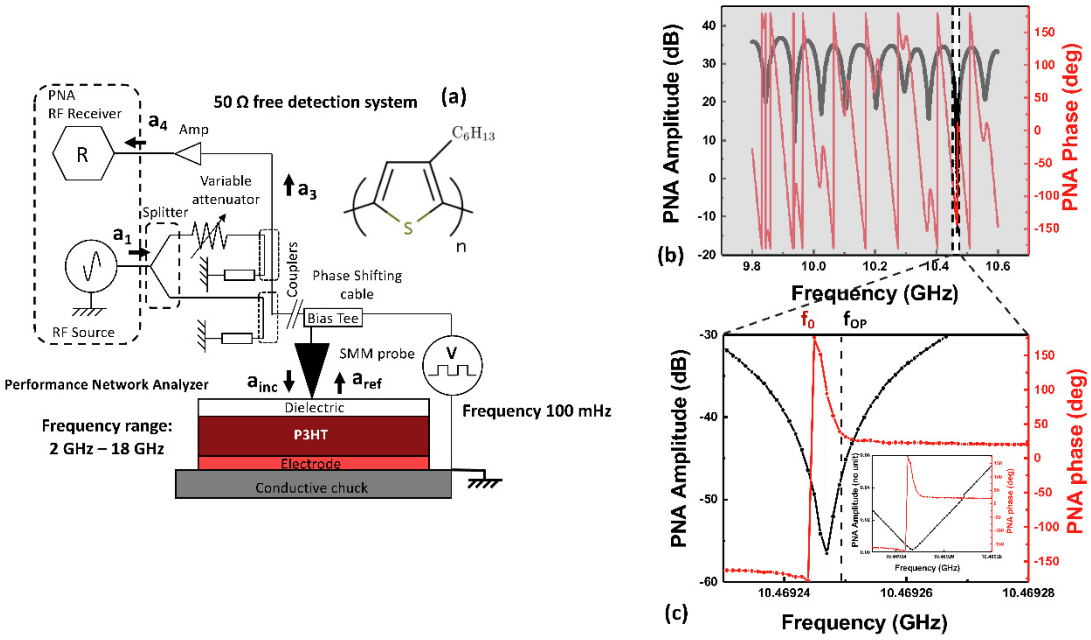

Figure 1. (**a**) Schematic of the Keysight SMM set-up augmented with the Mach-Zehnder interferometer for 50 Ω free detection system. The sample Metal/Insulator/Semiconductor (MIS) architecture is also depicted along of the chemical structure of the reference material studied (P3HT). (**b**,**c**) Typical interferometric performance network analyzer (PNA) Amplitude and Phase profiles recorded across the samples described in (**a**) in broad and narrow bandwidth at the interferometric frequency, respectively. f_0 and f_{OP} stand for the interferometric minimum amplitude and operating frequencies, respectively. The profiles in (**c**) are shown in semi-Log scale, and in linear scale in the inset.

3. Results and Discussion

3.1. Measurement Artifacts

Figure 2a shows the PNA phase (pale red) and amplitude (grey) interferometric profiles recorded prior to bias variations, while Figure 2b shows the variations for a fixed frequency of operation of both the PNA Amplitude and Phase signals upon DC step bias between 0 V and −2.5 V applied at the tip at a frequency of 100 mHz (10 s period) and in a time frame of 100 s (10 cycles). The interferometric frequency f_0 was initially measured at 10.469247 GHz (the light grey profile at t_0), while the operating one f_{OP} was set to 10.469249 GHz, i.e., 2 kHz higher (the right side of the interferometric profile). A low drift, estimated in this case to be around 23 Hz s^{-1} and inherent to the interferometric detection unit, induced a slow and continuous increase in f_0 with time. The time profiles displayed in Figure 2b were captured sufficiently later to be in the situation $f_0 > f_{OP}$ (between t_1 and $t_1 + \Delta t$, with $\Delta t = 100$ s, and $t_1 - t_0 = 442$ s). Hence the phase values between 170° and 180° and both the PNA phase and amplitude signals increasing with time as the drift further shifts the interferometric towards higher frequencies. Figure 2a displays in black and dark gray the reconstructed amplitude, and in red and paler red the reconstructed phase interferometric profiles at the beginning (t_1) and the end of the time profile ($t_1 + \Delta t$) assuming the sole drift as disturbing artifacts. At f_{OP}, now on the left side of the interferometric profile, the two profiles barely differ in phase while the bias average PNA amplitude increases within a 2 dB range as observed in Figure 2b. Along with the frequency shift, additional minor distortions of the interferometric profiles are also observed. These distortions are exemplified in Figure S1 (S stands for supplementary). This figure shows the superimposition of the PNA amplitude interferometric profile of Figure 2a (t_0) with the corresponding one recorded after the capture of the time profiles ($t_0 + 711$ s > $t_1 + \Delta t$). The drift is compensated to stress that the perturbations are limited in the close vicinity of f_0 (grey zone in Figure S1, i.e., in a spectral range ±5 kHz around f_0 thus lying away of the f_{OP} ranges. These perturbations can therefore be disregarded in the following analysis.

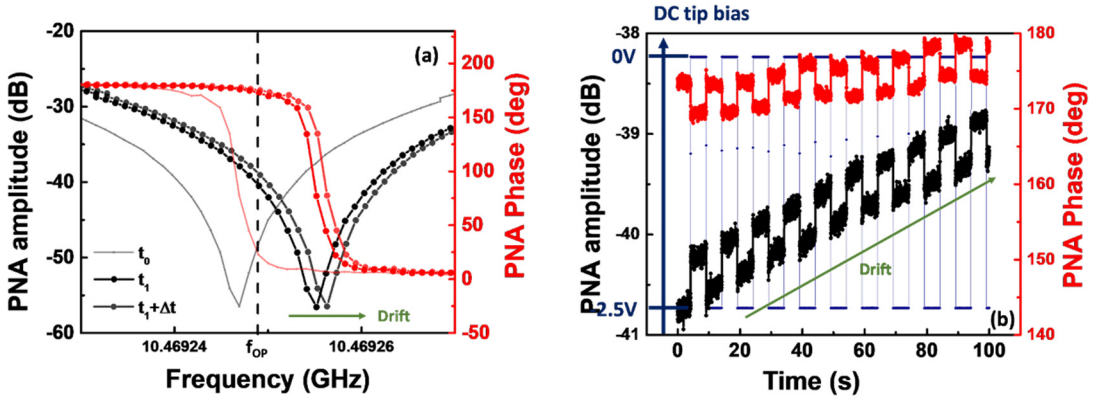

Figure 2. (**a**) PNA Amplitude and Phase spectra captured at t_0. The spectra at t_1 and $t_1 + \Delta t$ corresponding to the interferometric response prior to and after the capture of time profiles displayed in (**b**) are reconstructed from the spectra at t_0 taking only into account the drift of f_0 evaluated ~1.7 Hz s^{-1} (**b**) Variations of PNA Amplitude and Phase upon DC gate bias for f_{OP}~10.4925 GHz. The applied DC tip bias is also shown associated with a vertical blue scale.

3.2. Variations of PNA Signals with Bias

As a negative tip bias is applied, both PNA amplitude and phase signals exhibit variations. In Figure 2b, a −2.5 V DC tip bias leads to a decrease (increase) in the amplitude (phase) signal. This suggests a sensitivity of SMM and the ability of S_{11} to detect variations of electrical properties of P3HT as negative DC tip bias favors hole injection in the P3HT from the bottom electrode. Comparative measurements displayed in Figure S2 but with $f_{OP} > f_0$ exhibit reversed amplitude and phase variations with −3 V DC bias. It is worth noting that in addition to $f_{OP} > f_0$, the 180° shift at the interferometric frequency is also opposite that in Figure 2a. In other words, because the amplitude and phase profiles are both decreasing functions with frequency when $f_{OP} < f_0$ like in Figure 2a, if the biasing was inducing only a frequency shift of f_0, one should observe this frequency shift with in phase amplitude and phase variations (i.e., increasing or decreasing together). A similar reasoning can be made in Figure S2 where the amplitude and phase profiles are both increasing around $f_{OP} > f_0$. Therefore, a frequency shift upon bias cannot be the only signature of the bias on the PNA signals.

To further investigate the origin of the amplitude and phase variations at $f_{OP} < f_0$ upon biasing, Figure 3a,b evidence the impact of the bias onto the PNA amplitude and phase interferometric profiles, respectively. At the inset of both figures, a broad range display of the PNA signal is shown, highlighting in green the narrower spectral range in which f_{OP} is usually set and which corresponds to the main display. Several interferometric profiles were successively captured varying the bias progressively from 0 V to −6 V. A last record at 0 V allows for a determination of the inherent drift towards higher frequencies as mentioned before and confirmed in Figure 3a between the black and grey profile. Despite the drift, one can clearly observe the significant decrease (increase) in the amplitude (phase) signal with the bias consistent with what observed in Figure 2a in similar $f_{OP} < f_0$ operating conditions. The inset in Figure 3a also shows an increase in the interferometric fringe at −6 V that could be responsible for the decrease in the amplitude signal. Meanwhile, the apparent decrease in the amplitude signal at −6 V is more pronounced for $f_{OP} < f_0$ compared to $f_{OP} > f_0$ operating conditions. This indicates that DC bias induces both a frequency shift and variations in the fringe amplitude of the interferometric profiles. These mechanisms are likely to be cross linked in the time profiles observed before, unless f_{OP} is properly chosen, so that frequency shift and fringe amplitude variations more specifically impact the PNA amplitude and phase, respectively.

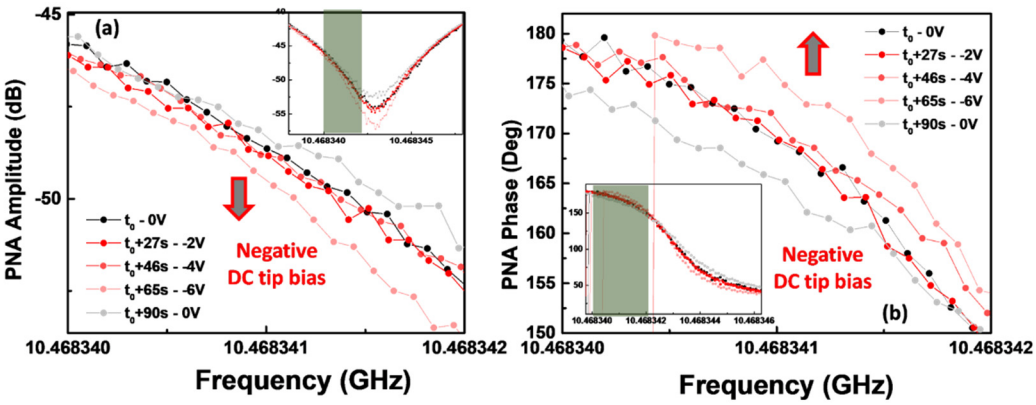

Figure 3. Interferometric PNA amplitude (**a**) and phase (**b**) profiles highlighting their respective sensitivity to negative DC tip bias in operating conditions $f_{OP} < f_0$. The bias induces in (**a**) a displacement of the interferometric fringe towards lower frequencies and, in this case, a deepening of the interferometric amplitude fringe, while in (**b**) a steepening of the phase profiles is observed. Hence, upon bias a decrease in the amplitude and an increase in the phase signals are observed at f_{OP}, respectively. In insets, the different amplitude and phase spectra across a wider range including f_0. For each profile at $t > t_0$ the frequency shift (~+7 Hz s^{-1}) was artificially compensated to allow better observation of the variations of both PNA signals with negative DC tip bias. The highlighted spectral range of the profiles corresponds to the green area in their respective insets.

Figure S3 shows interferometric and associated time profiles of PNA phase and amplitude captured upon the time at the same fringe around 10.46944 GHz. Once the probe came into contact with the sample, a first interferometric profile was captured (top black and red curves in Figure S3a, t_0), followed by two time profiles with a step bias of −1 V and $f_0 > f_{OP}$ (Figure S3b). Without lifting up the probe, but tuning the interferometer, the protocol of capture of interferometric was repeated (bottom black and red curve in Figure S3a, t_0 + 829 s) followed by time profiles with step bias of −1 V, −2 V and −3 V and $f_{OP} > f_0$ (black/pink, grey/red and pale grey/pale red amplitude/phase profiles in Figure S3c). In Figure S3b,c, at −1 V, negligible echo of the step bias could be observed in the amplitude time profiles, but only in the phase ones. This suggests that several mechanisms can be probed upon bias variations, being more sensitively detected by the amplitude or the phase signals. In Figure S3c, however, at −3 V, an artefact occurring at ~20 s in the time profiles is simultaneously detected by both amplitude and phase signals, also indicating possible crosstalk between the signals. In Figure S3b,c, profiles differ from f_{OP} and their relative value compared to f_0 and the fringe amplitude of the interferometric profiles. Very high fringe amplitude (Figure S3c) is likely to exhibit high variations upon small perturbations like that of DC bias. Both phase and amplitude signals are then expected to significantly vary in the very narrow spectral range with $f_{OP} \approx f_0$, thus leading to as observed cross-talking between the signals. Conversely, lower fringe amplitude even $f_{OP} \approx f_0$ will limit the impact of its variations with bias to the only PNA phase, thus allowing other mechanisms to be detected upon bias in PNA amplitude. Interestingly, consistent amplitude variations between Figure 2b and Figure S2b and other profiles (not shown) can be explained by a frequency shift towards lower frequency upon negative DC tip bias. Meanwhile, consistency between Figure 2b, Figures S2b and S3b could also be observed between phase signals, considering variations towards a $-\pi$ phase shift at f_0. The results reported by Seki et al. on benzothiophene derivative exposed to 9 GHz in a dielectric resonator also discriminated between a frequency shift and Q-factor variations of the S_{11} upon bias at the resonance frequency of the cavity, and attributing them to variations of the complex permittivity of the material under test, i.e., the dielectric constant and the loss (thus the conductivity), respectively [13]. Here, the variations of the 180° phase shift at f_0 upon bias can be correlated to a more pronounced imbalance between the two branches of the interferometer initially set to compensate the pathway probing with the reference one. In general, the effect of electrical perturbations on interferences and resonances cannot be so easily

correlated. Resonances result from multiple interferences. They can be modeled by an equivalent RLC circuit. Therefore, their frequency shift can be related to a variation in capacitance or inductance and the Q-factor is related to the resistance or more generally to energy loss phenomena. In contrast, interferences represent the sum of two phase-shifted monochromatic signals with similar amplitudes. Although the amplitude in log scale near the minimum may look as a resonance, in linear scale, it looks like a sinus function (Figure 1c, inset) with a minimum that will actually reach the residual thermal noise signal if the amplitudes of the two shifted signals are exactly the same. The perturbation of the signal on one branch by the change of the impedance-induced wave reflection unbalances the interference which results in a variation of the amplitude and phase of the measured signal. However, qualitatively, this mechanism presents some analogy with the Q-factor variations observed by Seki et al. in their resonator and attributed to specific bias induced loss, hence conductivity variations. Their observed frequency shift is attributed to permittivity variations induced by charge trapping. The existing analytical models supporting SMM systems augmented with a Mach-Zehnder interferometer-based detection unit [15], once applied to the above results displayed in Figure S3b, may attribute PNA amplitude and phase signals to capacitance and conductivity. Quantitative evaluation of the variations of these parameters usually lie in the order of the aF and the μS, respectively [15]. More precise determination, however, must precisely consider the operating setpoint (f_{OP}) regarding the interferometric profiles (f_0) to fix the sensitivity of the measurement. Figure S3b shows two sets of time profiles captured successively applying a −1 V step bias. As the interferometric drift further moves away the operating setpoint compared to f_0, the mean PNA amplitude (phase) increased (decreased) in the second profile while the variations of the PNA phase with bias are also less pronounced. This must also be taken into account in interpreting Figure S3c, for which the significant increase in phase variations with bias is a combination of the drift (opposite to that of Figure S3c since here $f_0 < f_{OP}$) and the injection of carriers the P3HT.

3.3. Material Properties Probing

Previous studies involving microwave probing of semiconducting polymers by means of so-called voltage modulated microwave spectroscopy and flash-photolysis time-resolved microwave conductivity also observed conductivity increase in the upon voltage or light excitation of the polymer [10,11]. They determined local carrier mobility, attributing their measurements to properties taking place at the mesoscopic scale, and more precisely to polymer intrachain charge transport. The formation of polarons upon light absorption or carrier injection with different excited states associated with the carrier could be discriminated by the energy formation and relaxation dynamics. Strong electric field was also shown to extend the diffusion of carriers along the chain by enhancing hopping rates at potential barriers induced by defects in the chain, and therefore improving carrier transport. Polarons are charge-phonon coupling and are shown to drive intramolecular transport mechanisms in organic semiconductors [29,30]. In polymers, polaron assisted transport therefore corresponds to intrachain carrier motion. Many different polarons can be considered with materials and structures. Descriptive formalism is acknowledged [31] and polaron lifetime usually ranges from fs to ns [32,33], allowing spectroscopic characterization from THz down to GHz. Existing measurements report higher carrier mobility compared to conventional low frequency bulk probing methods, typically three to four orders of magnitude ~10^0 cm^2 V^{-1} s^{-1}. As conjugation drives the carrier motion, intrachain transport is simpler compared to interchain [34,35]. Here, existing analytical modelling tools, as proposed in SI, allow for local variations of conductivity ~μS to be determined. These could be coarsely explained from $G = e.p.\mu.S/d$, with G the measured conductance, e the elementary charge, p the carrier density in accumulated P3HT ~10^{18} cm^{-3} [28], μ the intrachain mobility ~10^0 cm^2 V^{-1} s^{-1} [10], S the contact area ~50×50 nm^2 and d the penetration depth d ~25 nm, much lower than the film thickness (~150 nm), consistently with the chosen frequency ~10.5 GHz sufficiently high to limit the microwave penetration depth to a fraction of the semiconductor thickness (See Figure S4a,b).

In their dielectric resonator configuration, Seki et al. attributed the observed frequency shift of microwave power spectrum to variations of dielectric constant induced by the contribution of trapped

carriers in the measurements [13]. In SMM, as illustrated in Figure S4, the penetration depth of the microwave, decreases with both the operating frequency and the conductivity of the probed volume. Upon negative bias, carrier accumulation increases the loss and reduces the penetration depth of the microwave in the P3HT. This indirectly increases the corresponding capacitance between the tip contact and the conductivity plan at the maximum penetration depth of the microwave (See Figure S4a,b). Consequently, negative biasing would have combined impact of both the frequency shift and the sharpness of the interferometric fringes as shown in Figures 2 and 3 and Figure S2. Especially, a decrease (increase) in the penetration depth (capacitance) upon negative bias corresponds to a frequency shift towards lower values. The analytical model proposed in S6 estimated the capacitance variations of a few aF. With the proposed dimensions above, and $\delta C = -\frac{\varepsilon_0 \varepsilon_r}{d^2}.S.\delta d$ with $\varepsilon_0 \varepsilon_r$ the dielectric permittivity of the material, δC~1 aF variations of capacitance correspond to δd~10 nm.

As PNA signal variations with bias are expected to be the signature of polarons with high mobility, the above analysis is also consistent with identical sharp transient response in amplitude and phase time profiles (see Figure 2b and Figure S2b).

Meanwhile, the contribution of traps could also be observed. This requires lower frequency operation to probe a deeper volume and a large tip bias. The SMM probing depth and the variations of the material electrical properties upon bias are depicted in Figure S5c,d. Associated experimental results are displayed in Figure S5. Figure S5a shows the interferometric response across a fringe with minimum frequency f_0 chosen around 3.5709 GHz with an operating set up $f_{OP} > f_0$ to minimize drift induced perturbations during measurement. Figure S5b displays the corresponding PNA amplitude and phase time profiles and their variations with bias. The phase signal decreases with bias consistently, with variations of the interferometric profile towards a $+\pi$ shift of the signal at f_0. Like previous phase profiles, sharp transient variations are also observed with bias. This suggests again a charge increase in P3HT upon bias forming polaron in the probed volume and whose fast dynamics cannot be resolved by the VNA controller. On the contrary, transient mechanisms can clearly be observed in the PNA amplitude time profile. These transient discrepancies between phase and amplitude profiles confirm that different mechanisms can be probed simultaneously with SMM and be discriminated between the two signals. The amplitude decreases with more negative bias, indicating now a frequency shift towards higher values. Therefore, the origin of the drift can no longer attributed to contractions of the probed volume upon conductivity increase. The observed transient with characteristic time around 10 s upon bias variations would rather be attributed to carrier trapping/detrapping mechanisms. As illustrated in Figure S4c,d, the low frequency operating microwave is now probing the whole semiconducting film. Upon the bias, no variations of the penetration depth can occur. However, the large electric field across the field is likely to empty hole deep traps in the P3HT at the back contact. This can explain the shift towards higher frequencies of the PNA amplitude, corresponding to a decrease in probed capacitance, while the slow transient characteristics describe their peculiar dynamics.

4. Conclusions

In summary, SMM equipped with a Mach-Zehnder interferometer to allow for 50 Ω free detection system and probing high impedance semiconducting materials was applied to electrically characterize P3HT as a reference semiconducting polymer in a Metal-Insulator-Semiconductor structure. The microwave probing method operating in a 2 to 20 GHz spectral range was shown to be sensitive to variations of electrical properties in the semiconductor upon negative DC tip bias. Provided the operating setpoint is appropriately adjusted in the vicinity of a chosen interferometric fringe to ensure enough sensitivity ($|f_{OP} - f_0| < 100$ kHz) and avoid cross-talking artifacts ($|f_{OP} - f_0| > 10$ kHz), PNA phase and amplitude signal variations could be simultaneously and independently correlated to the conductive and capacitive mechanisms modifying the properties of P3HT upon bias. High frequencies occurred to be more efficient for the study of intrachain conductive mechanisms associated with the formation of polarons along polymer chains and generated from carrier injection upon bias, and for the determination of locally charged transport mechanisms and associated mobilities. Low frequencies

probing locally across the whole material appeared more suitable to explore trapping mechanisms inherent to the morphology of organic semiconductors. This study evidenced the versatility of SMM but also the necessary constraints for efficient experimental protocols to carry out high resolution non-contact electrical characterization of organic semiconductors, to be useful both for the fundamental understanding of physical mechanisms at stake in these complex materials and for the industrial development of organic electronics.

Supplementary Materials: The following are available online at http://www.mdpi.com/2076-3417/10/22/8234/s1, Figure S1: Complement to interferometric profiles of Figure 2, Figure S2: Complement to interferometric and time profiles of Figure 2, Figure S3: additional interferometric and associated time profiles at 10.46944 GHz, Figure S4: Schematic of the variations of the tip sample interactions varying microwave frequency and probed bias, Figure S5: interferometric and associated time profiles at 3.5709 GHz, S6: Interferometer modeling.

Author Contributions: Conceptualization, O.D., D.T. and D.M.; methodology, O.D., D.T. and D.M. validation, O.D., D.T. and D.M.; formal analysis, O.D., D.T. and D.M.; investigation, O.D., D.T. and D.M.; resources, O.D., D.T.; writing—original draft preparation, O.D.; writing—review and editing, O.D., D.T. and D.M.; supervision, O.D.; All authors have read and agreed to the published version of the manuscript.

Funding: This work was supported by the European Union's Horizon 2020 Research and Innovation Programme under Grant Agreement No. 761036 (MMAMA project) and by the National Research Agency (ANR) under the project EQPX ExCELSiOR.

Conflicts of Interest: The authors declare no conflict of interest.

References

1. Inganäs, O. Organic Photovoltaics over Three Decades. *Adv. Mater.* **2018**, *30*, e1800388. [CrossRef] [PubMed]
2. Perovskites for Optoelectronics, Nature Reviews in Nature Research. 2019. Available online: https://www.nature.com/collections/fnnxcznnbb/content/reviews (accessed on 19 November 2020).
3. Bin, H.; Gao, L.; Zhang, Z.-G.; Yang, Y.; Zhang, Y.; Zhang, C.; Chen, S.; Xue, L.; Yang, C.; Xiao, M.; et al. 11.4% Efficiency non-fullerene polymer solar cells with trialkylsilyl substituted 2D-conjugated polymer as donor. *Nat. Commun.* **2016**, *7*, 13651. [CrossRef] [PubMed]
4. Holliday, S.; Ashraf, R.S.; Wadsworth, A.; Baran, D.; Yousaf, S.A.; Nielsen, C.B.; Tan, C.-H.; Dimitrov, S.D.; Shang, Z.; Gasparini, N.; et al. High-efficiency and air-stable P3HT-based polymer solar cells with a new non-fullerene acceptor. *Nat. Commun.* **2016**, *7*, 11585. [CrossRef] [PubMed]
5. Vlahacos, C.P.; Black, R.C.; Anlage, S.M.; Amar, A.; Wellstood, F.C. Near-field scanning microwave microscope with 100 µm resolution. *Appl. Phys. Lett.* **1996**, *69*, 3272–3274. [CrossRef]
6. Tuteja, M.; Koirala, P.; Palekis, V.; MacLaren, S.; Ferekides, C.S.; Collins, R.W.; Rockett, A.A. Direct Observation of CdCl2Treatment Induced Grain Boundary Carrier Depletion in CdTe Solar Cells Using Scanning Probe Microwave Reflectivity Based Capacitance Measurements. *J. Phys. Chem. C* **2016**, *120*, 7020–7024. [CrossRef]
7. Brinciotti, E.; Gramse, G.; Hommel, S.; Schweinboeck, T.; Altes, A.; Fenner, M.A.; Smoliner, J.; Kasper, M.; Badino, G.; Tuca, S.-S.; et al. Probing resistivity and doping concentration of semiconductors at the nanoscale using scanning microwave microscopy. *Nanoscale* **2015**, *7*, 14715–14722. [CrossRef]
8. Berweger, S.; Macdonald, G.A.; Yang, M.; Coakley, K.J.; Berry, J.J.; Zhu, K.; DelRio, F.W.; Wallis, T.M.; Kabos, P. Electronic and Morphological Inhomogeneities in Pristine and Deteriorated Perovskite Photovoltaic Films. *Nano Lett.* **2017**, *17*, 1796–1801. [CrossRef]
9. Gramse, G.; Kölker, A.; Škereň, T.; Stock, T.J.Z.; Aeppli, G.; Kienberger, F.; Fuhrer, A.; Curson, N.J. Nanoscale imaging of mobile carriers and trapped charges in delta doped silicon p–n junctions. *Nat. Electron.* **2020**, *3*, 1–8. [CrossRef]
10. Martens, H.; Hilt, O.; Brom, H.B.; Blom, P.W.; Huiberts, J.N. Voltage-Modulated Millimeter-Wave Spectroscopy on a Polymer Diode: Mesoscopic Charge Transport in Conjugated Polymers. *Phys. Rev. Lett.* **2001**, *87*, 086601. [CrossRef]
11. Saeki, A.; Seki, S.; Sunagawa, T.; Ushida, K.; Tagawa, S. Charge-carrier dynamics in polythiophene films studied by in-situ measurement of flash-photolysis time-resolved microwave conductivity (FP-TRMC) and transient optical spectroscopy (TOS). *Philos. Mag.* **2006**, *86*, 1261–1276. [CrossRef]
12. Plassard, C.; Bourillot, E.; Rossignol, J.; Lacroute, Y.; Lepleux, E.; Pacheco, L.; Lesniewska, E. Detection of defects buried in metallic samples by scanning microwave microscopy. *Phys. Rev. B* **2011**, *83*. [CrossRef]

13. Choi, W.; Tsutsui, Y.; Sakurai, T.; Seki, S. Complex permittivity analysis revisited: Microwave spectroscopy of organic semiconductors with resonant cavity. *Appl. Phys. Lett.* **2017**, *110*, 153303. [CrossRef]
14. Wang, F.; Clément, N.; Troadec, D.; Legrand, B.; Dambrine, G.; Théron, D. Nanoscale capacitors study with an interferometric scanning microwave microscope. In Proceedings of the Materials Research Society Fall Meeting, MRS Fall 2013, Symposium LL: Advances in Scanning Probe Microscopy, Boston, MA, USA, 1–6 December 2013.
15. Haddadi, K.; Polovodov, P.; Théron, D.; Dambrine, G. Quantitative Error Analysis in Near-Field Scanning Microwave Microscopy. In Proceedings of the 2018 International Conference on Manipulation, Automation and Robotics at Small Scales (MARSS), Nagoya, Japan, 4–8 July 2018. [CrossRef]
16. Oladipo, A.O.; Lucibello, A.; Kasper, M.; Lavdas, S.; Sardi, G.M.; Proietti, E.; Kienberger, F.; Marcelli, R.; Panoiu, N.C. Analysis of a transmission mode scanning microwave microscope for subsurface imaging at the nanoscale. *Appl. Phys. Lett.* **2014**, *105*, 133112. [CrossRef]
17. Li, J.; Nernati, Z.; Haddadi, K.; Wallace, D.C.; Burke, P.J. Scanning Microwave Microscopy of Vital Mitochondria in Respiration Buffer. In Proceedings of the 2018 IEEE/MTT-S International Microwave Symposium—IMS, Philadelphia, PA, USA, 10–15 June 2018. [CrossRef]
18. Gao, C.; Wei, T.; Duewer, F.; Lu, Y.; Xiang, X.-D. High spatial resolution quantitative microwave impedance microscopy by a scanning tip microwave near-field microscope. *Appl. Phys. Lett.* **1997**, *71*, 1872–1874. [CrossRef]
19. Huber, H.P.; Moertelmaier, M.; Wallis, T.M.; Chiang, C.J.; Hochleitner, M.; Imtiaz, A.; Oh, Y.J.; Schilcher, K.; Dieudonne, M.; Smoliner, J.; et al. Calibrated nanoscale capacitance measurements using a scanning microwave microscope. *Rev. Sci. Instrum.* **2010**, *81*, 113701. [CrossRef] [PubMed]
20. Lai, K.; Ji, M.; Leindecker, N.; Kelly, M.A.; Shen, Z.X. Atomic-force-microscope-compatible near-field scanning microwave microscope with separated excitation and sensing probes. *Rev. Sci. Instrum.* **2007**, *78*, 063702. [CrossRef] [PubMed]
21. Hoffmann, J.; Gramse, G.; Niegemann, J.; Zeier, M.; Kienberger, F. Measuring low loss dielectric substrates with scanning probe microscopes. *Appl. Phys. Lett.* **2014**, *105*, 013102. [CrossRef]
22. Lai, K.; Kundhikanjana, W.; Kelly, M.A.; Shen, Z.X. Calibration of shielded microwave probes using bulk dielectrics. *Appl. Phys. Lett.* **2008**, *93*, 123105. [CrossRef]
23. Gramse, G.; Kasper, M.; Fumagalli, L.; Gomila, G.; Hinterdorfer, P.; Kienberger, F. Calibrated complex impedance and permittivity measurements with scanning microwave microscopy. *Nanotechnology* **2014**, *25*, 145703. [CrossRef]
24. Berweger, S.; Weber, J.C.; John, J.; Velazquez, J.M.; Pieterick, A.; Sanford, N.A.; Davydov, A.V.; Brunschwig, B.; Lewis, N.S.; Wallis, T.M.; et al. Microwave Near-Field Imaging of Two-Dimensional Semiconductors. *Nano Lett.* **2015**, *15*, 1122–1127. [CrossRef]
25. Imtiaz, A.; Wallis, T.; Kabos, P. Near-Field Scanning Microwave Microscopy: An Emerging Research Tool for Nanoscale Metrology. *IEEE Microw. Mag.* **2014**, *15*, 52–64. [CrossRef]
26. Kundhikanjana, W.; Lai, K.; Wang, H.; Dai, H.; Kelly, M.A.; Shen, Z.-X. Hierarchy of Electronic Properties of Chemically Derived and Pristine Graphene Probed by Microwave Imaging. *Nano Lett.* **2009**, *9*, 3762–3765. [CrossRef] [PubMed]
27. Toth, D.; Hailegnaw, B.; Richheimer, F.; Castro, F.; Kienberger, F.; Scharber, M.C.; Wood, S.; Gramse, G. Nanoscale charge accumulation and its effect on carrier dynamics in tri-cation perovskite structures. *ACS Appl. Mater. Interfaces* **2020**. [CrossRef] [PubMed]
28. Moerman, D.; Sebaihi, N.; Kaviyil, S.E.; Leclère, P.; Lazzaroni, R.; Douheret, O. Towards a unified description of the charge transport mechanisms in conductive atomic force microscopy studies of semiconducting polymers. *Nanoscale* **2014**, *6*, 10596–10603. [CrossRef]
29. Lu, N.; Li, L.; Geng, D.; Liu, M. A review for polaron dependent charge transport in organic semiconductor. *Org. Electron.* **2018**, *61*, 223–234. [CrossRef]
30. Asadi, K.; Kronemeijer, A.J.; Cramer, T.; Koster, L.J.A.; Blom, P.W.M.; De Leeuw, D.M. Polaron hopping mediated by nuclear tunnelling in semiconducting polymers at high carrier density. *Nat. Commun.* **2013**, *4*, 1710. [CrossRef]
31. Lu, N.; Li, L.; Banerjee, W.; Sun, P.; Gao, N.; Liu, M. Charge carrier hopping transport based on Marcus theory and variable-range hopping theory in organic semiconductors. *J. Appl. Phys.* **2015**, *118*, 045701. [CrossRef]

32. Li, K.; Shen, Y.; Majumdar, N.; Hu, C.; Gupta, M.C.; Campbell, J.C. Determination of free polaron lifetime in organic bulk heterojunction solar cells by transient time analysis. *J. Appl. Phys.* **2010**, *108*, 084511. [CrossRef]
33. Wang, T.; Caraiani, C.; Burg, G.W.; Chan, W.-L. From two-dimensional electron gas to localized charge: Dynamics of polaron formation in organic semiconductors. *Phys. Rev. B* **2015**, *91*, 041201. [CrossRef]
34. Noriega, R.; Rivnay, J.; Vandewal, K.; Koch, F.P.V.; Stingelin, N.; Smith, P.; Toney, M.F.; Salleo, A. A general relationship between disorder, aggregation and charge transport in conjugated polymers. *Nat. Mater.* **2013**, *12*, 1038–1044. [CrossRef]
35. Yao, Y.; Dong, H.; Liu, F.; Russell, T.P.; Hu, W. Approaching Intra- and Interchain Charge Transport of Conjugated Polymers Facilely by Topochemical Polymerized Single Crystals. *Adv. Mater.* **2017**, *29*, 1701251. [CrossRef] [PubMed]